



HAL
open science

An original interferometric study of NGC 1068 with VISIR BURST mode images

Anne Poncelet, C. Doucet, Guy Perrin, Hélène Sol, Pierre-Olivier Lagage

► **To cite this version:**

Anne Poncelet, C. Doucet, Guy Perrin, Hélène Sol, Pierre-Olivier Lagage. An original interferometric study of NGC 1068 with VISIR BURST mode images. *Astronomy and Astrophysics - A&A*, 2007, 472, pp.823-831. 10.1051/0004-6361:20067012 . hal-03796944

HAL Id: hal-03796944

<https://hal.science/hal-03796944>

Submitted on 5 Oct 2022

HAL is a multi-disciplinary open access archive for the deposit and dissemination of scientific research documents, whether they are published or not. The documents may come from teaching and research institutions in France or abroad, or from public or private research centers.

L'archive ouverte pluridisciplinaire **HAL**, est destinée au dépôt et à la diffusion de documents scientifiques de niveau recherche, publiés ou non, émanant des établissements d'enseignement et de recherche français ou étrangers, des laboratoires publics ou privés.

An original interferometric study of NGC 1068 with VISIR BURST mode images[★]

A. Poncelet^{1,2}, C. Doucet³, G. Perrin², H. Sol¹, and P. O. Lagage³

¹ LUTH, Observatoire de Paris, 92195 Meudon Cedex, France
e-mail: anne.poncelet@obspm.fr

² LESIA, Observatoire de Paris, 92195 Meudon Cedex, France

³ CEA/DSM/DAPNIA/Service d'Astrophysique, CE Saclay, 91191 Gif-sur-Yvette, France

Received 22 December 2006 / Accepted 22 June 2007

ABSTRACT

Context. We present 12.8 μm images of the core of NGC 1068, the archetype Seyfert type II galaxy, obtained during first operations of the *BURST mode* of the VLT/VISIR (Imager and Spectrometer in the InfraRed at the Very Large Telescope).

Aims. We trace structures under the diffraction limit of one UT (Unit Telescope at the VLT) and we investigate the link between dust in the vicinity of the central engine of NGC 1068, recently resolved by interferometry with MIDI (Mid-Infrared Interferometer), and more extended structures. This step is mandatory for a multi-scale understanding of the sources of mid-infrared emission in active galactic nuclei (AGN).

Methods. A speckle processing of VISIR *BURST mode* images was performed to extract very low spatial-frequency visibilities, first considering the full field of VISIR *BURST mode* images and then limiting it to the mask used for the acquisition of MIDI data.

Results. Extracted visibilities are reproduced with a multi-component model. We identify two major sources of emission at 12.8 μm : a compact one <85 mas, directly associated with the *dusty torus*, and an elliptical one of size (<140) mas \times 1187 mas and PA $\sim -4^\circ$ (from north to east), which gives a new description of the NS elongation of the nucleus. This is consistent with previous deconvolution processes.

The combination with MIDI data reveals the close environment of the *dusty torus* to contribute to $\sim 83\%$ of the MIR flux seen by MIDI.

Conclusions. This strong contribution has to be considered in modeling long baseline interferometric data. It must be related to the NS elongated component which is thought to originate from individually unresolved dusty clouds located inside the ionization cone which are photoevaporating and radiatively accelerated. Low temperatures of the *dusty torus* are not challenged, emphasizing the scenarios of clumpy torus.

Key words. galaxies: individual: NGC 1068 – galaxies: Seyfert – galaxies: active – techniques: image processing – techniques: interferometric – instrumentation: high angular resolution

1. Introduction

NGC 1068, a bright and near archetype Seyfert type II galaxy is a key target in testing the unified scheme of active galactic nuclei (AGN). This stipulates that Seyfert II and Seyfert I are the same objects, depending upon the inclination of the nucleus along the line of sight (Antonucci & Miller 1985). The *dusty torus* is therefore an important element of this paradigm. The most recent theoretical models are given by Nenkova et al. (2002), Schartmann et al. (2005), Hönig et al. (2006), Elitzur & Shlosman (2006), among others.

Multi-wavelength observations of the nucleus of NGC 1068 have been reviewed by Galliano et al. (2003). Recently, deconvolution of near-IR adaptive optics (AO) images of NGC 1068 shows an unresolved core of some 30 mas along the NS axis and <15 mas along the EW axis (in the K_s band). Additionally, upper size limits of 50 mas in the L' and M' bands were set (Gratadour et al. 2006). These data also exhibit an ~ 800 mas extended, peculiar S-shaped distribution aligned with the radio

jet. Near-IR speckle interferometry has revealed a component of $FWHM \sim 18$ mas \times 39 mas oriented at PA $\sim -16^\circ$ (Weigelt et al. 2004). Combined with the VLT/VINCI measurement of (Wittkowski et al. 2004), data were fitted with two components of $FWHM < 5$ mas and 40 mas. The first MIR images reported by Bock et al. (2000) traced the same NS elongation of the nucleus, and the 12.8 μm deconvolved images from the VLT/VISIR (Galliano et al. 2005) highlights several knots distributed along the S-shape (twisting from PA = -4° to PA = 31°). Using mid-IR spectroscopy, Mason et al. (2006) distinguished two sources of mid-IR emission, a compact core within the central $0'.4 \times 0'.4$ and a more extended component linked to heated dust inside the ionization cone. Mid-IR interferometric observations with the VLT/MIDI were necessary to resolve the *dusty torus* of NGC 1068. The first data were obtained in 2003 and presented by Jaffe et al. (2004). Two independent analyses have revealed a compact structure of dust composed of amorphous silicates, with size <82 mas and relatively low temperatures (on the order of 350 K; Jaffe et al. 2004; Poncelet et al. 2006).

Configurations of Unit Telescopes (UTs) at the VLTI do not provide baselines shorter than 30 m, although low spatial-frequency visibility points would yield tight constraints for

[★] Based on commissioning time observations collected at the ESO/Paranal MELIPAL telescope.

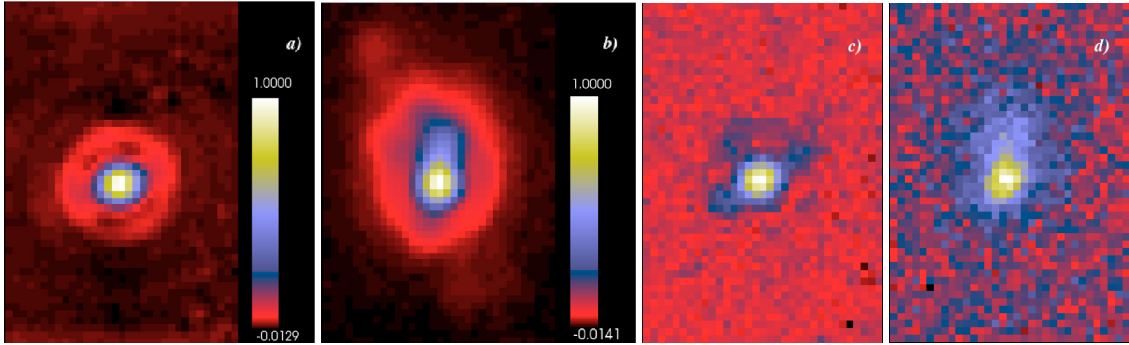


Fig. 1. 12.8 μm images obtained with the *BURST mode* of VISIR. For comparison, normalized images are displayed with the same color table. *From left to right:* **a)** sum of the 2200 individual exposures on HD 11383 (reference star). The good signal-to-noise ratio has to be compared to individual exposures. Here we clearly see the Airy disk (~ 10.5 pixels large centered on the brightest pixel). **b)** Sum of the 13 000 exposures obtained on NGC 1068. The full structure appears clearly: the NS elongation from the unresolved compact core, the asymmetric emission and a knot farther away toward the NE (north is up and east is left). The apparent EW elongation is due to the diffraction ring at ~ 393 mas from the core. **c)** Example of an individual 16 ms exposure of HD 11383. The Airy disk faintly appears, attesting to the good seeing conditions during the night of observation. **d)** An individual exposure of NGC 1068, already showing the NS elongation of the nucleus.

modeling MIDI data. One way to at least partially solve this problem is to observe with a single UT to access baselines between 0 and 8.2 m (the pupil of one UT) using an interferometric processing of images.

NGC 1068 was observed at 12.8 μm in January 2005 using the *BURST mode* (or quasi-Speckle mode) of VISIR. The big advantage of this is the shorter acquisition time of 16 milliseconds, far shorter than the typical atmospheric turbulence variations of ~ 300 ms at 10 μm . The aim of the study is therefore to present the *BURST mode* of VISIR to show its advantages and its use for the speckle analysis. This allows us to derive the mid-IR low spatial-frequency visibilities between 0 and 8 m of baseline for the first time. Next we compare these to MIDI data points in order to establish the link between the source of mid-IR emission on different scales. Section 2 gives details on the *BURST mode* of VISIR and presents the principle of how visibilities are extracted from VISIR images. Results of the modeling applied to the VISIR visibilities are shown and discussed in Sect. 3. Section 4 presents the link between VISIR and MIDI observations. Section 5 gives the general conclusions drawn by this study.

2. Observations and data processing

NGC 1068 was observed on the night of January 25, 2005 using the *BURST mode* of VISIR, which is installed on the VLT (Paranal, Chili). The actual observation mode used is described in Doucet et al. (2006). Total exposure time on the object was 208 seconds using the 12.8 μm Ne II filter ($\Delta\lambda = 0.21 \mu\text{m}$). The exposure time was 16 ms for individual images. The airmass was ~ 1.20 at the time of observations. HD 11383, a K5III spectral type star, was observed as a calibrator. To correct for the turbulence with offline processing, data are stored every 1000 elementary images for one nodding position, using a chopping frequency of 0.25 Hz in the NS direction. After classical data reduction in the mid-IR range, a cube of 500 images, both chopped and nodded (4 beams/image), is obtained. Turbulence has the effect of moving each of the 4 sources independently so they have to be individually extracted from the cube. Finally images of similar quarter are shifted and added, producing some 13 000 and 2200 elementary images of NGC 1068 and HD 11383, respectively. To obtain a better signal-to-noise ratio – and according to the good correlation between elementary images – they

are added in blocks of 5 (the sums may be considered as instantaneous maps of the source intensity). Individual and resulting 12.8 μm VISIR *BURST mode* images of NGC 1068 and of HD 11383 may be found in Fig. 1.

The *BURST mode* is important because it uses such a short exposure time that it effectively freezes atmospheric turbulence. Therefore it enabled us to apply the speckle technique first introduced by Labeyrie (1970) as an analytical tool. This aims to reach the diffraction limit of a large telescope (i.e. ~ 320 mas at 12.8 μm), after incoherent integration of exposures.

The seeing was excellent and very stable during observations of NGC 1068 and images are diffraction-limited. Thus, the monochromatic transfer function $\tilde{T}_\lambda(u, v)$ is estimated well by observations of the calibrator star. Unbiased visibilities for NGC 1068 and for the calibrator star are computed from the power spectra of the images:

$$\begin{aligned} |V_{\text{calib}}(u, v)|^2 &= \langle |\tilde{I}_{\text{calib}}(u, v)|^2 \rangle_t - \langle |\tilde{N}_{\text{calib}}(u, v)|^2 \rangle_t \\ |V_{\text{NGC 1068}}(u, v)|^2 &= \langle |\tilde{I}_{\text{NGC 1068}}(u, v)|^2 \rangle_t - \langle |\tilde{N}_{\text{NGC 1068}}(u, v)|^2 \rangle_t \end{aligned} \quad (1)$$

where $\tilde{I}_{\text{NGC 1068}}$, \tilde{I}_{calib} , $\tilde{N}_{\text{NGC 1068}}$, and \tilde{N}_{calib} are the Fourier transforms of the normalized intensity distribution on individual VISIR *BURST mode* images of NGC 1068, of the calibrator star, and of the background photon noise on the related images, respectively. The final calibrated visibility estimate is

$$|V(u, v)|^2 = \frac{|V_{\text{NGC1068}}(u, v)|^2}{|V_{\text{calib}}(u, v)|^2}. \quad (2)$$

In our study, the most important interest of *BURST mode* observations compared to long-time exposures is the ability to calibrate the source spatial spectrum. We considered error propagation to determine error bars for the uncalibrated visibilities. A Monte-Carlo computation is used to estimate error bars for the calibrated visibility. It consists in generating random numbers with a Gaussian distribution for $|V_{\text{NGC 1068}}|^2$ and $|V_{\text{calib}}|^2$ (as the histograms of the individual exposure estimates are Gaussians) taking their standard deviations into account. The standard deviation of the simulated visibility distribution is the 1σ error on $|V(u, v)|^2$. Depending on spatial frequencies, error bars on visibilities range between 1 and 10%. Two-dimension (2D) maps of the visibilities and associated error bars are obtained. Because the intensity distribution of the source is real, this 2D visibility map is centro-symmetric with respect to the zero spatial frequency (see left of Fig. 2). Cuts of the map along several orientations are

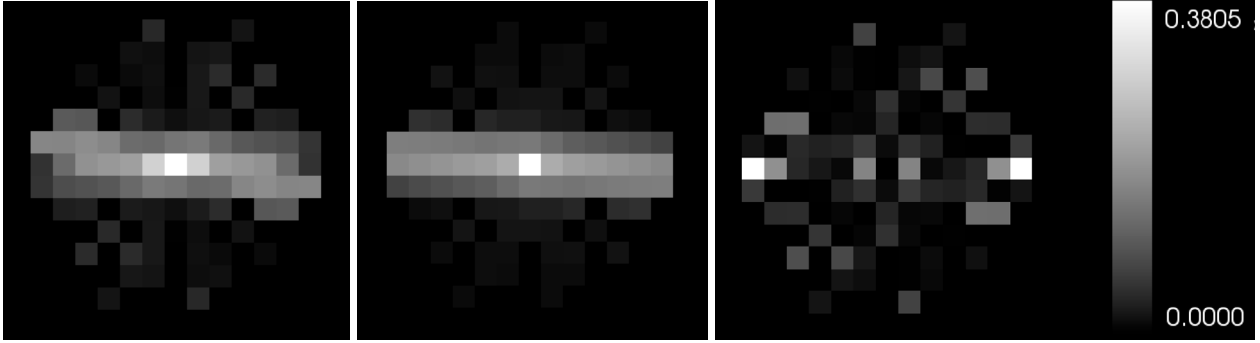


Fig. 2. *Left:* visibility map as extracted from *BURST* mode VISIR images. Only data points used for fits have value, others are set to 0. *Middle:* visibility map from the model of two circular disks and one elliptical uniform one (reduced $\chi^2 = 8.7$). These two maps are scaled between 0 and 1 (white points corresponding to a visibility value of 1 and black ones to value of 0). Comparison between left and right illustrates the quality of the fit. *Right:* map of absolute terms of residuals, i.e. subtraction of the modeled visibility map to the measurements one. The color scaling of the residuals map is presented on the right side.

presented in Fig. 3. Orientations of the spatial frequency plane correspond to the orientation on the sky plane (conventions used being 0° is related to the NS axis and 90° to the EW axis in images).

In the following, the visibilities are compared to simple geometrical models as is often the case in optical-infrared interferometry. A model of the spatial brightness distribution of the source $O(\alpha, \delta)$ is used to extrapolate the high-spatial frequency information from the measured low spatial frequencies. Thus, thanks to the a priori information injected through this model, structures smaller than the diffraction limit of the instrument can be estimated. This super-resolution technique works as long as the signal-to-noise ratio on visibilities is high enough to be able to detect a visibility drop with respect to 1. In classical imaging, an equivalent technique consists in detecting the width difference between the point spread function (psf) and the source intensity peak. This requires a high signal-to-noise ratio, however, and an excellent stability of the psf.

3. First study of VISIR visibilities

In this section, visibilities are compared to uniform disk models that we used as rulers for measuring the typical sizes of structures in the object as a function of azimuth. The complexity of models increases to account for the whole evolution of the visibility and especially for the departure from a circular symmetry.

3.1. Modeling

3.1.1. Azimuth-dependent modeling

The 2D visibility map derived from VISIR images (see left of Fig. 2) shows an elongated shape in a direction close to 90° . Similarly, cuts of this map along different orientations (see Fig. 3) highlight the steep fall in visibility along the NS axis (see plots corresponding to 0° in Fig. 3) in comparison with the perpendicular axis (see plots corresponding to 90°). The higher the visibility, the smaller the observed source. The source is then well-resolved along the NS axis and smaller as we look towards the perpendicular axis. A minimum of two uniform disks in the model is necessary to fit the different cuts of visibilities. For each orientation (marked by θ), the free parameters associated with the model are the sizes of the two disks ($\varnothing_1(\theta)$ and $\varnothing_2(\theta)$) and the flux ratio between them ($\eta(\theta)$). Fits are presented in Fig. 3. Along each direction, optimum parameters were evaluated with

a χ^2 minimization and error bars on parameters were obtained by varying the χ^2_{\min} by 1. The global value of the reduced χ^2 (i.e. corresponding to all fits) is given by

$$\chi_{\text{red}}^2 = \frac{1}{N - P_1} \sum_{i=1}^N \left[\frac{V_i^2 - M_i(\varnothing_1(\theta), \varnothing_2(\theta), \eta(\theta))}{\sigma_i} \right]^2 \quad (3)$$

where $(N - P_1)$ is the number of degrees of freedom, N stands for the number of visibility points ($N = 91$), and P_1 is the number of free parameters. There are 3 parameters per orientation and a total of 12 orientations ($P_1 = 36$), V_i and σ_i are respectively visibilities and error bars measured with the speckle analysis, M_i are the modeled visibility values. The value of the global reduced χ^2 is 24.9. The size of the inner component is <300 mas, below the diffraction limit of the UT. The second component is well-resolved (~ 1600 mas) and more or less circularly symmetric. For each component, sizes and error bars related to each orientation are reported in the image and linked for the extended one (left panel in Fig. 4). Nevertheless, it is difficult to figure out the real shape of the components since part of the asymmetry is due to the azimuth dependence of the flux ratio between the two components. It ranges between ~ 0.29 along the EW axis and ~ 4.76 along PA = 14° from N to E. A more realistic description of MIR sources in the nucleus of NGC 1068 is given by the global modeling explained below.

3.1.2. Global modeling

Using our previous results, we attempted to produce a global fit of all orientations at the same time using a more complex model. The global fit of the 2D map of VISIR was based on the most reliable visibility points (see left of Fig. 2). We here consider the flux ratio between the components to be a constant. To account for the asymmetry of the visibility distribution, we first made use of a simple model of one circular, plus one elliptical, uniform disk. This model converges to two different kinds of solutions with an equivalent value of the reduced $\chi^2 = 27$. This value is equivalent to the one obtained with the previous model applied to each direction independently. It turns out that an additive component was mandatory to have a better fit of the visibility map and to better constrain the upper size limit of the smallest component. To limit the number of parameters and account for the asymmetry of the visibility map, this third model consists in two circular uniform disks plus an elliptical one. There are seven free

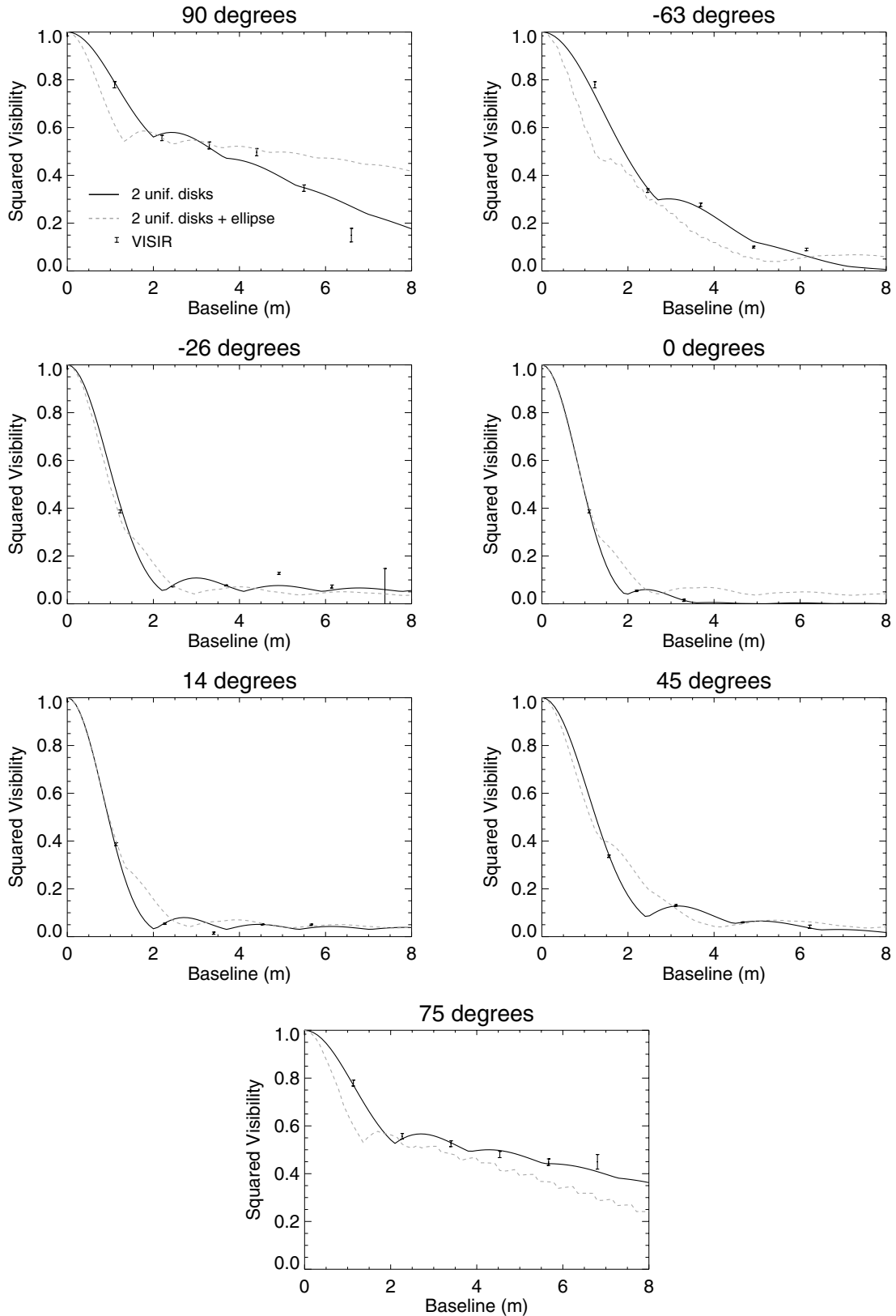


Fig. 3. VISIR visibilities derived from *BURST mode* images at $12.8 \mu\text{m}$ and associated error bars (symbols) along several directions (angles are positive from north to east). One can see the softer fall of the visibility toward the EW axis (90°) than toward the NS axis (0°), highlighting the NS elongation of the source. *Black solid line* corresponds to fits with the two circular uniform disk model independently applied for each orientation (global $\chi^2_{\text{red}} \sim 24.9$). *Dashed grey line* corresponds to the last model considered consisting in two circularly and one elliptical uniform disk. This model is used in order to fit all baselines simultaneously. The value of the reduced χ^2 is here 8.7. It is smaller than the value related to the previous model due to the higher number of freedom degrees of the global model (see Sect. 3.1).

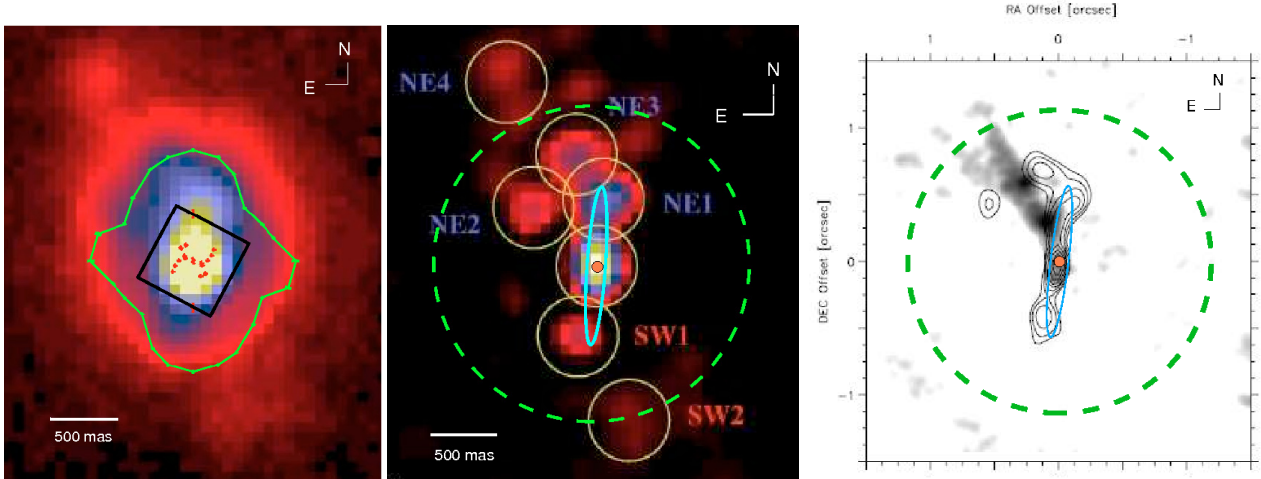


Fig. 4. *Left:* comparison of different contributions to MIR emission in the core of NGC 1068. Background is the resulting $12.8 \mu\text{m}$ VISIR *BURST mode* image. Sizes derived from the two uniform disks model applied to each orientation and as described in Sect. 3.1.1 are superposed (*red and green components*). The *black square* displays the MIDI mask considered in the second part of the study of VISIR visibilities (see Sect. 4). *Middle:* comparison between the structures resulting from the global modeling presented in Sect. 3.1.2 and the deconvolved image obtained from VISIR standard-mode observations (Galliano et al. 2005). *Right:* same comparison with the contour plot of the $12.5 \mu\text{m}$ deconvolved image obtained at Keck 2 (Bock et al. 2000) and the 5GHz radio map of Gallimore et al. (2004) (grey scale). *Green dashed lines* correspond to the more extended component. The *blue ellipse* corresponds to the elongated one at PA $\sim -4^\circ$, of size (<140) mas \times 1187 mas. The *orange innermost component* represents the inner uniform disk <85 mas. This component is directly associated to the *dusty torus* resolved in interferometry with MIDI (Jaffe et al. 2004; Poncelet et al. 2006).

parameters: the diameter of the two circular disks (\varnothing_1 and \varnothing_2); the semi-major and the semi-minor axes a and b , and the orientation θ of the elliptical disk in the sky plane (angles are positive from north to east); the flux ratios between the small and intermediate components (η_1) and between the intermediate and the largest one (η_2).

$$\chi_{\text{red}}^2 = \frac{1}{N - P_2} \sum_{i=1}^N \left[\frac{V_i^2 - M_i(\varnothing_1, \varnothing_2, a, b, \theta, \eta_1, \eta_2)}{\sigma_i} \right]^2 \quad (4)$$

where $N = 91$ and $P_2 = 7$.

The minimization of the previous expression of the reduced χ^2 yields the following constraints on the parameters:

- $\varnothing_1 < 85$ mas
- $a < 140$ mas
- $b = 1187 \pm 22$ mas
- $\theta = -3.7 \pm 0.8^\circ$
- $\varnothing_2 = 2367 \pm 107$ mas
- $\eta_1 = 3.0 \pm 0.1$
- $\eta_2 = 1.4 \pm 0.1$.

Values for θ_1 and a are close to zero. We chose to give an upper limit for these parameters as 0 is within the 1σ range of uncertainty. The corresponding modeled visibility and residuals maps are presented in the middle and on the right of Fig. 2, respectively. Fits of visibilities by this model for different orientations in the (u, v) plane are compared to the ones obtained with the first model of two circularly uniform disks in Fig. 3. The reduced χ^2 is equal to 8.7. It is smaller than with the first model for which the number of degrees of freedom was much larger.

For comparison with previous observations, geometrical parameters constrained by this model are shown on the deconvolved image of Galliano et al. (2005) and Bock et al. (2000) (see the middle and right panels of Fig. 4). The compact core and the ellipse account for the core and the NS elongation (i.e. knots NE1 and SW1 of Galliano et al. 2005), while the 2.4 uniform disk accounts (both in size and total brightness) for the

background of fainter structures at larger scales. The comparison shows the consistency of the different processings applied to MIR images obtained at Keck 2 and with VISIR at the VLT.

3.2. Discussion of the results

3.2.1. The MIR core

The speckle analysis provided a constraint in size, i.e. an upper limit of ~ 85 mas for the inner source of emission in the nucleus. This is well below the diffraction limit of the UT at $12.8 \mu\text{m}$ (i.e. 320 mas) or the *FWHM* upper limits of 290 and 190 mas (along the NS and EW directions respectively), which are measured from deconvolution of the $12.8 \mu\text{m}$ image obtained with the standard acquisition mode of VISIR (Galliano et al. 2005).

This structure is directly associated with the *dusty torus* first resolved by interferometry using MIDI. It is in good agreement with sizes produced by studies from both Jaffe et al. (2004, *FWHM* < 49 mas) and Poncelet et al. (2006, diameter < 82 mas). The present study does not allow any questions to be addressed about the orientation or inclination of this dust structure. However, evidence from H_2O maser disks inclined at -45° (Greenhill & Gwinn 1997) is thought to indicate the location of the inner edge of the *dusty torus* (Kartje et al. 1999). This orientation has subsequently been confirmed by the analysis of recent MIDI observations (Jaffe et al. 2006), so we adopted it in Fig. 5.

In the NIR, the K-band core has been found to measure $18 \text{ mas} \times 39 \text{ mas}$ oriented at PA $\sim 16^\circ$ (Weigelt et al. 2004). This orientation differs from both the MIR and the distribution of water masers. Likewise, deconvolved NACO images from Gratadour et al. (2006) trace structures ~ 30 mas and < 15 mas in the K-band along the NS and EW axes, respectively. This K-band structure is thought to be associated to the inner edge of the *dusty torus*, which is heated by radiation from the central engine.

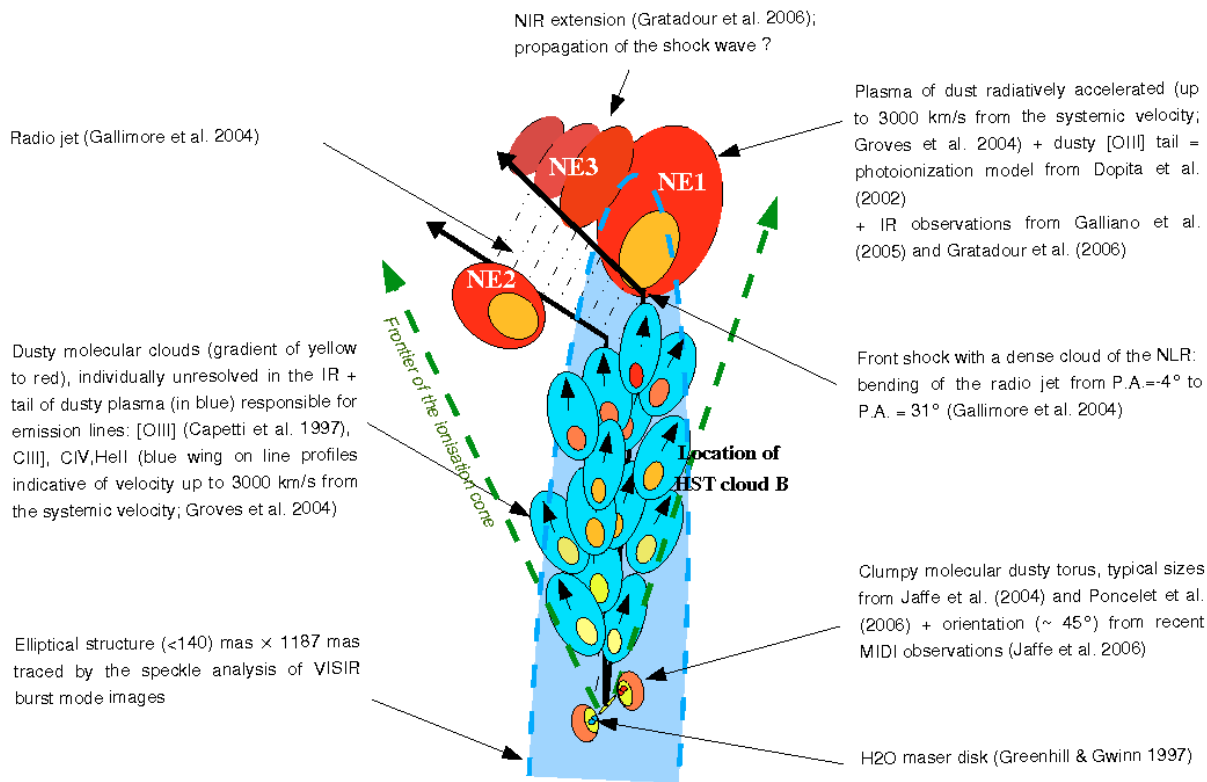


Fig. 5. Picture summarizing the multi-wavelength structures observed toward the north in the nucleus of NGC 1068, as discussed in Sect. 3.2.2. Among others, the representation of the radio jet (which bends from PA = -4° to PA = 31°) comes from observations of Gallimore et al. (2004), H₂O masers from Greenhill & Gwinn (1997), the *dusty torus* from Jaffe et al. (2004), Poncelet et al. (2006) and Jaffe et al. (2006), MIR clouds from the present study and from Galliano et al. (2003), NIR emission from Gratadour et al. (2006), [OIII] clouds from Capetti et al. (1997), and UV lines from Groves et al. (2004). The yellow color was chosen for heated dust, the gradient of yellow to red color is used for decreasing dust temperature (typically ranging between 300–500 K) and blue color for [OIII] UV clouds, for which HeII, CIII], and CIV emission-line profiles have a pronounced blue wing indicative of proper motion up to -3000 km s^{-1} , meaning that they are moving toward us. The blue elliptical structure derived from the analysis of VISIR *BURST mode* images is discussed in Sect. 3.2.2.

3.2.2. The NS elongated structure

The (<140) mas \times 1185 mas elliptical structure is aligned with the base of the radio jet in the AGN of NGC 1068 (PA $\sim -4^\circ$). The ellipse matches both the NE1 and SW1 knots of the deconvolved image of Galliano et al. (2005, see middle panel in Fig. 4). The knot sizes are roughly equal to the diffraction limit of the telescope so they must be understood as upper size limits. In our case thanks to the super-resolution brought about by the interferometric analysis technique, the elliptical disk is thinner. Moreover, the deconvolution process of Galliano et al. (2005) may have emphasized the intensity fluctuations in the structure just enough to produce the knots. On this basis, our ellipse must be viewed as an average model of these knots. Therefore, it is difficult to say which of the two source representations is the best, but it should be noted that the superimposition of the ellipse and contour plot from deconvolved $12.5 \mu\text{m}$ images from Bock et al. (2000) is very striking (see right panel of Fig. 4). Our model does allow us to interpret a fraction of the flux of the central knot as part of the elongated structure, whilst the remaining fraction belongs to the central core (left unresolved by the image). Flux ratios between the different components are discussed in Sect. 3.2.4.

Examining the other wavelengths provides strong evidence for a correlation between the NS extended core and HST [OIII] clouds A and B (the location of HST cloud B is marked in Fig. 5, Capetti et al. 1997) located at $0'.1$ S and N of the core,

respectively. The NIR observations of Gratadour et al. (2006) and fainter levels of flux observed on the deconvolved images of Galliano et al. (2005) suggest no depletion of dust in the region between the core and knot NE1.

The silicate feature evolution from the core up to $\pm 3''$ outwards has been investigated by Rhee & Larkin (2006) and Mason et al. (2006). Rhee & Larkin (2006) interpret this trend as dust emission from the inner edge of the *dusty torus*. If this is correct it would mean that the torus should extend up to $1''$ in the EW direction, however neither interferometry nor VISIR observations have shown this to be true. Indeed molecular dust has been found inside the ionization cone up to 600 mas toward the N of the central engine (Mason et al. 2006). Thus drawing upon the conclusion of Mason et al. (2006) and using the theoretical work of Dopita et al. (2002), we explain our elliptical structure and the correlation between the NIR, MIR, and UV emissions in the nucleus of NGC 1068 in terms of unresolved small clouds and of molecular dust irradiated and photoionized by strong X/UV radiation fields produced by the central engine. Dust at the front is directly heated by X-rays then photoevaporates and generates a hot plasma of dust. This in turn is radiatively accelerated away from the central engine and emits in both NIR and MIR. In addition an envelope of ionized gas is produced that would account for the narrow emission lines in the UV and optical ranges. It would also explain the distribution of [OIII] clouds. This interpretation is strengthened by HST spectroscopy (Groves et al. 2004) that shows that the CIII], CIV, and HeII UV

line profiles have a pronounced blue wing within this region. This is associated with the proper motions of velocities up to 3000 km s^{-1} , which are indicative of NLR clouds being pushed toward us. Fits of these line ratios point towards photoionization as the dominating mechanism in comparison with excitation by radio-jet/interstellar medium shocks. Thus, NLR dusty clouds observed in NIR, MIR, UV must be at the front of the ionization cone and accelerated towards us in a radiative wind (see Fig. 5). The thinness of the ellipse can then be explained either by the ionization cone having a very small opening angle $\lesssim 50^\circ$ (i.e. the angle between the two frontiers of the ionization cone), meaning that the opening angle of the torus would be $\gtrsim 150^\circ$ (i.e. the angle between northern and southern walls of the torus) or by the motion of the small unresolved dusty clouds being frozen in that of the radio jet. In both cases, their propagation would have to be confined to a thin region, such as what is observed.

The effects of jet-NLR clouds interactions are weak on the UV spectra (Groves et al. 2004) so could not account for the high color temperature observed in the NIR range so far away from the central engine (Gratadour et al. 2006). However, it is striking that the elongated ellipse is aligned with the radio jet close to the core. There is actually some evidence for local jet-NLR interactions, such as the bending of the jet axis initially at PA = -4° to PA = 31° (Gallimore et al. 2004). This would indicate a direct collision between the radio jet and a dense NLR cloud – labeled HST-C in UV (Capetti et al. 1997), NE1 in MIR (Galliano et al. 2005), and IR-1b in the NIR (Gratadour et al. 2006). A twisting of structures involving these two PA is found in the deconvolved MIR and NIR images (Galliano et al. 2005; Gratadour et al. 2006). The peculiar distribution of knots above cloud NE1 may be the signature of the shock-wave propagation in the dusty plasma medium as already discussed by Gratadour et al. (2006). The global picture of this scenario is given in Fig. 5.

3.2.3. More extended structures

The extended component of the model of the VISIR visibilities has been used to account for the most extended contributions to the flux. Given the deconvolved image of Galliano et al. (2005), it includes knots NE2, NE3, NE4 and SW2 (see the middle panel of Fig. 4). The geometry we considered is clearly too simple, but a detailed description of the extended environment of the core of NGC 1068 goes beyond the scope of the present study. The important information to consider here is the flux ratios between the total flux from the extended environment and from the inner structures.

3.2.4. Flux ratios between components

We compare the flux ratios values from our global modeling, equal to 3 and 1.4 between the different components, with observations of Bock et al. (2000) and Galliano et al. (2005). First, our inner component is associated to the source of flux labeled *b* in Fig. 5 of Bock et al. (2000) and the ellipse (referred to *elongated* component in the following) to those labeled *a* and *c*. According to their mean fluxes, we deduce $F_{\text{core}}/F_{\text{elongated}} = 2.92$. This ratio is in very good agreement with our best fit.

Then, using Table 1 of Galliano et al. (2005) and associating both our elongated component with the SW1 and NE1 knots and our extended uniform disk with the remaining SW and NE knots, we have computed the following flux ratios:

- $F_{\text{core}}/F_{\text{elongated}} = 2.02$
- $F_{\text{elongated}}/F_{\text{extended}} = 1.72$.

Given the uncertainties on photometry measurements in deconvolved images and the simplicity of our model, and considering that the structures of Galliano et al. (2005) are large in size compared to the diffraction limit of the telescope, these ratios are in good agreement with those derived from our study. Since the elongated structure in the EW direction and the central core are not resolved by the telescope, both fluxes are biased, and this can explain part of the discrepancy between the two estimates.

We conclude that our simple interferometric model has captured most of both the sizes and relative intensities of the object structures when compared to the deconvolved images. It offers extra information thanks to the higher resolution achieved, both on the core associated to the dusty torus and on the width of the NS elongated structure.

4. Comparison with MIDI observations

4.1. How to compare VISIR and MIDI visibilities ?

One of the important aims of the study is the link between low spatial-frequency visibilities derived from VISIR images, with long baselines data points obtained with MIDI and the radiative transfer model by Poncelet et al. (2006). Visibilities extracted in part 2 correspond to a field of view for VISIR of several arcseconds, whilst the field of view for MIDI is limited to a slit of $0'.6 \times 2''$ oriented at -30° . In addition, the emerging flux is mainly limited to what comes from the core by a $\sim 0'.6 \times 0'.6$ mask oriented at -30° centered on the nucleus (left panel of Fig. 4).

In processing images such as the conditions of MIDI observations we first unbias spectra from the pixelization of VISIR images, and secondly we take the mask of MIDI into account. To correctly position the mask on the flux maximum, we have to keep the spatial information of images contained in the phase of spectra (in addition of the unbiased moduli). New spatial spectra of NGC 1068 and the calibrator are then calculated via the following equations:

$$S_{\text{NGC 1068}}(u, v) = |V_{\text{NGC 1068}}(u, v)| \times e^{-i \Phi_{\text{NGC1068}}} \quad (5)$$

$$S_{\text{calib}}(u, v) = |V_{\text{calib}}(u, v)| \times e^{-i \Phi_{\text{calib}}} \quad (6)$$

where $|V_{\text{NGC 1068}}(u, v)|$ and $|V_{\text{calib}}(u, v)|$, $\Phi_{\text{NGC 1068}}$ and Φ_{calib} are respectively the moduli unbiased from noise (as calculated in Sect. 2) and the phases of the spatial spectra of NGC 1068 and of the calibrator star.

The bias produced from pixelization effects is corrected by dividing moduli by the pixel transfer function in the Fourier plane, the pixel being considered as a simple filter with a width of 75 mas (i.e. the size of one pixel) in the image plane. For oversampling, original 32×32 maps are padded out with zeros after the cut-off frequency of the UT (i.e. D/λ), to achieve 256×256 maps. The resulting maps produce new pixels angular size of $\sim 9.4 \text{ mas pixels}^{-1}$. The MIDI mask coded onto a 256×256 image is Fourier transformed. Spectra of NGC 1068 and of the calibrator star are convolved with the spectrum of the mask, written as

$$S_{\text{mask}}(u, v) = |V_{\text{mask}}(u, v)| \times e^{-i \Phi_{\text{mask}}}. \quad (7)$$

Low spatial-frequency visibilities derived from VISIR images as obtained in the same conditions of MIDI data acquisition are given by

$$|V(u, v)| = \frac{|S_{\text{NGC1068}}(u, v) * S_{\text{mask}}(u, v)|}{|S_{\text{calib}}(u, v) * S_{\text{mask}}(u, v)|} \quad (8)$$

where * stands for the convolution.

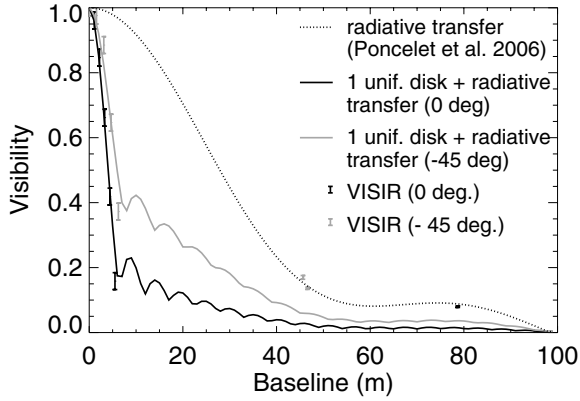


Fig. 6. Comparison between high spatial-frequency visibilities from MIDI at $12.8 \mu\text{m}$ (data points at 45 and 78 m) and low spatial frequency ones derived from VISIR *BURST mode* images including the mask discussed in Sect. 4 (points between 0 and 8 m of baseline). The model of the two uniform disks (*black and grey solid lines*) has to be compared with the radiative transfer model of Poncelet et al. (2006) applied to MIDI data (*black dotted line*). A third component has been added to the one already revealed by the radiative transfer, to partially account for the steep fall of the visibility at short baseline. Size of this component is ~ 600 mas and ~ 300 mas along directions oriented at 0° and -45° respectively.

MIDI observations made in 2003 correspond to baselines oriented at 0° and -45° . Therefore only cuts along these two orientations of low spatial-frequency visibility maps have been retained. For individual exposures, signal-to-noise ratio is low and phases are noisy. Therefore error bars on visibilities are not computed from the statistical distribution of individual measurements as in Sect. 2, but from the reduced χ^2 of fits at 0° (see Fig. 7), which has been forced to be equal to 1. It is equivalent to considering the model as correct and to interpreting discrepancies with the data as errors. This leads to a qualitative estimate of the error of ~ 0.026 , which has been applied to all visibilities between 0 and 8 m. The comparison with MIDI data points is presented in Fig. 6.

4.2. The link between MIDI and VISIR observations

Figure 6 is the comparison between *a)* low spatial-frequency visibilities from VISIR images considering the MIDI mask, *b)* high spatial frequency ones from MIDI, and *c)* the model of Poncelet et al. (2006) that reproduces MIDI data. The unexpected sharp fall of low spatial frequencies visibilities demonstrated how constraining these measurements are for modeling long baseline interferometric data.

On the one hand, short baselines visibilities are well-reproduced by a uniform disk model of sizes ~ 450 mas and ~ 350 mas along directions at 0° and -45° , respectively. On the other hand, high spatial-frequency visibilities from MIDI are represented by a radiative transfer model inside a dusty layer ranging in size between 35 mas and 82 mas (Poncelet et al. 2006). The initial attempt to fit both sets of data simultaneously was associated with the model of the dusty layer of Poncelet et al. (2006) being surrounded by a uniform disk. The only free parameters were the size of the uniform disk and the flux ratio between the disk and the dusty layer. This model agrees with the strong fall of visibility at low projected baselines but fails to account for the faint level of visibility at high projected baselines (see Fig. 6). This forces us to attempt a new fit in which we have to consider the parameters of the dusty layer of

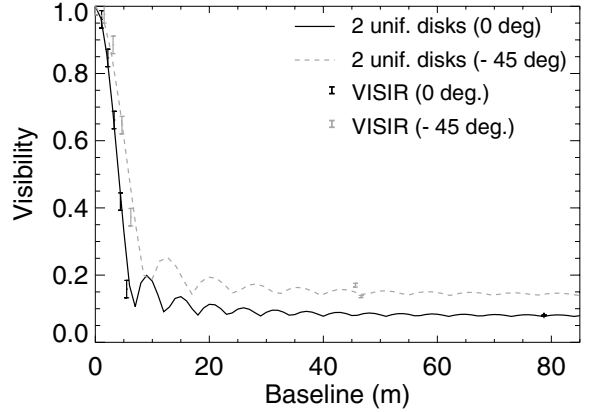


Fig. 7. Comparison between high spatial-frequency visibilities from MIDI at $12.8 \mu\text{m}$ and low spatial frequency ones derived from VISIR *BURST mode* images including the MIDI mask as discussed in Sect. 4. *Solid black and dashed grey lines* correspond to a model of two circularly uniform disks applied along both directions at 0° and -45° independently. Optimum parameters are: $\varnothing_1(0^\circ)$ and $\varnothing_1(-45^\circ) < 21$ mas, $\varnothing_2(0^\circ) = 479 \pm 17$ mas, $\varnothing_2(-4^\circ) = 450 \pm 9$ mas, $\eta(0 \text{ deg}) = 12 \pm 5$ and $\eta(-45^\circ) = 6 \pm 2$.

Poncelet et al. (2006) as free. This is not yet possible according to the limited amount of *BURST mode* data sets that are currently available, as the wider spectral range that is required.

Nevertheless, to be able to quantify the fraction of extended emission entering the field of view of MIDI, compared to the emission of the compact core, we fit both low and high spatial-frequency visibilities together in both directions using a simple model of two uniform disks, in which free parameters are the sizes and the flux ratios between the two disks. The minimum value of the reduced χ^2 is 3.42. This corresponds to an unresolved inner disk of upper size limit ~ 21 mas in each direction. The extended component has a size of 479 ± 17 mas along the NS direction and $\sim 350 \pm 9$ mas along $\text{PA} = -45^\circ$. The flux ratios between the two components are found to be 12 ± 5 and 6 ± 2 in these two directions (see fits in Fig. 7).

4.3. Discussion

This study demonstrates that there are two main structures appearing in the MIDI field of view, a compact one of size ~ 20 mas surrounded by an extended and slightly elongated one (the size ratio between -45° and 0° is $\sim 27\%$ for this second component). The first structure is associated to the dusty layer highlighted solely by the MIDI data (Jaffe et al. 2004; Poncelet et al. 2006). Sizes are slightly different due to the fact that it is a more simplistic model than those of Jaffe et al. (2004) and Poncelet et al. (2006). In addition, the direct environment surrounding the compact core (of size ~ 500 mas) that enters the field of view of MIDI was not taken into account by previous studies. According to the flux ratio between components, it contributes to more than 83% of the total flux seen by MIDI.

Constraints on temperatures of the *dusty torus* derived from only MIDI data (Poncelet et al. 2006) are not biased by this effect. Indeed they come from an additional information being the spectral energy distribution supplied by MIDI. They are found to be on the order of ~ 300 K, a value supported by the continuum slope of the central $0.4''$ *N*-band spectra (Mason et al. 2006). That temperatures are so low so close to the central engine is strong evidence of the clumpy nature of the *dusty torus* (Elitzur & Shlosman 2006).

The compact central component is already traced with the study of full field images presented in Sect. 3: it is directly associated to the innermost component <85 mas. The extended component, of sizes 479 ± 17 mas and 350 ± 9 mas along $PA = 0^\circ$ and -45° , is not entirely related to the elliptical NS elongated ellipse traced in Sect. 3.1.2 since this last one does not completely enter in the field of view of MIDI. However, according to the discussion in Sect. 3.2 and to the photoionization scenario of Dopita et al. (2002), this elongated component could be associated to small dusty clouds heated by the radiation field from the central engine and photoevaporating. The NIR and UV counterparts of these clouds (Gratadour et al. 2006; Capetti et al. 1997; Groves et al. 2004) and the evolution of the $9.7 \mu\text{m}$ silicate emission toward the north of the core (Mason et al. 2006) is evidence for the presence of dust inside the ionization cone at distances less than 300 mas from the central engine (i.e. half of the MIDI mask). The present study supports this fact and demonstrates the need to consider the close environment of the *dusty torus* for modeling interferometric data.

The small set of MIDI and VISIR BURST mode data currently available only allows the use of simple geometrical models for comparing low and high spatial-frequency visibilities. It is strongly necessary to apply this approach at different wavelengths to get a better description of the source of mid-IR emission seen by MIDI, associated with the dusty torus, and linked with its immediate surroundings.

5. Conclusions

The speckle analysis of the $12.8 \mu\text{m}$ BURST mode VISIR images constrains the upper size limit of the MIR core of NGC 1068 to 85 mas. This is well below the diffraction limit of the UT which demonstrates the *achievement* of the BURST mode of VISIR. The NS elongated component is described here as an elliptical structure oriented at $PA = -4^\circ$ (such as the base of the radio jet) and of size (<140) mas \times 1187 mas. Following the scenario proposed by Dopita et al. (2002), it is interpreted as small dusty clouds individually unresolved, distributed inside the ionization cone, and photoevaporating. This explains the correlation of observations at different wavelengths.

The use of VISIR BURST mode images for the comparison with MIDI data reveals the strong and unexpected fall in visibility between 0 and 6 m of baseline. The use of simple geometrical models accounts for the two data sets simultaneously and distinguishes between two main components: a compact one ~ 20 mas associated to the *dusty torus* traced by interferometry with MIDI (Jaffe et al. 2004; Poncelet et al. 2006) and an extended one (<500 mas) entering in the field of view of MIDI. This surrounding environment, partially related to the elongated elliptical structure, contributes to more than $\sim 83\%$ of the flux emitted by the core. It is therefore mandatory to take it into

account when modeling the MIDI data. By doing this we do not challenge the low temperatures of the *dusty torus* constrained by the previous analysis of MIDI data. Besides, it reinforces the scenarios of clumpy torus.

According to the small set of VISIR BURST mode and MIDI data available up to now, we reach the limits of simple descriptions of sources of mid-IR emission in the AGN of NGC 1068. To further describe the complexity of the compact dusty core and the deeper link with its direct surroundings, the same processing of VISIR BURST mode images has to be performed at other wavelengths. This will be possible when the BURST imaging mode of VISIR is open for observations at the VLT. Moreover, as it shows how constraining low spatial frequency visibility points are, this study underlines the need to further fill the gap of interferometric data between 8 and 45 m of projected baseline. On the one hand, baselines between 30 and 45 m are reachable with the VLTI and the UTs. On the other, since most of the ATs are now installed at Paranal, it will be interesting to attempt observations with these 1.8 m pupil telescopes to bridge the gap from 8 to 23 m to allow for more accurate multi-scale modeling of the inner part of NGC 1068.

Acknowledgements. We would like to thank Eric Thiebaut, Ferreol Soulez, and Renaud Foy for their help during the treatment of VISIR images.

References

- Antonucci, R. R. J., & Miller, J. S. 1985, ApJ, 297, 621
 Bock, J. J., Neugebauer, G., Matthews, K., et al. 2000, AJ, 120, 2904
 Capetti, A., Macchetto, F. D., & Lattanzi, M. G. 1997, ApJ, 476, L67
 Dopita, M. A., Groves, B. A., Sutherland, R. S., Binette, L., & Cecil, G. 2002, ApJ, 572, 753
 Doucet, C., Pantin, E., Lagage, P. O., & Dullemond, C. P. 2006, A&A, 460, 117
 Elitzur, M., & Shlosman, I. 2006, ApJ, 648, L101
 Galliano, E., Alloin, D., Granato, G. L., & Villar-Martín, M. 2003, A&A, 412, 615
 Galliano, E., Pantin, E., Alloin, D., & Lagage, P. O. 2005, MNRAS, 363, L1
 Gallimore, J. F., Baum, S. A., & O’Dea, C. P. 2004, ApJ, 613, 794
 Gratadour, D., Rouan, D., Mugnier, L. M., et al. 2006, A&A, 446, 813
 Greenhill, L. J., & Gwinn, C. R. 1997, Ap&SS, 248, 261
 Groves, B. A., Cecil, G., Ferruit, P., & Dopita, M. A. 2004, ApJ, 611, 786
 Hönl, S. F., Beckert, T., Ohnaka, K., & Weigelt, G. 2006, A&A, 452, 459
 Jaffe, W., Meisenheimer, K., Raban, D., Tristram, K., & Röttgering, H. J. A. 2006, in The Central Engine of Active Galactic Nuclei, ed. L. Ho, & J.-M. S. F. A. Wang
 Jaffe, W., Meisenheimer, K., Röttgering, H. J. A., et al. 2004, Nature, 429, 47
 Kartje, J. F., Königl, A., & Elitzur, M. 1999, ApJ, 513, 180
 Labeyrie, A. 1970, A&A, 6, 85
 Mason, R. E., Geballe, T. R., Packham, C., et al. 2006, ApJ, 640, 612
 Nenkova, M., Ivezić, Ž., & Elitzur, M. 2002, ApJ, 570, L9
 Poncelet, A., Perrin, G., & Sol, H. 2006, A&A, 450, 483
 Rhee, J. H., & Larkin, J. E. 2006, ApJ, 640, 625
 Schartmann, M., Meisenheimer, K., Camenzind, M., Wolf, S., & Henning, T. 2005, A&A, 437, 861
 Weigelt, G., Wittkowski, M., Balega, Y. Y., et al. 2004, A&A, 425, 77
 Wittkowski, M., Kervella, P., Arsenault, R., et al. 2004, A&A, 418, L39